REVIEW ARTICLE (INVITED ONLY)

Towards Stable, 30% Efficient Perovskite Solar Cells

Nam-Gyu Park[1,2] (ID)

Abstract

Solid-state perovskite solar cells (PSCs) were first discovered in 2012, where a power conversion efficiency (PCE) of 9.7% was demonstrated along with stability for 500 h at ambient atmosphere. Since then, the PCEs of PSCs have increased amazingly to over 26%. Moreover, perovskite/silicon tandem solar cells achieved a PCE as high as 34%. Such a superb photovoltaic performance is due to the inherent optoelectronic properties of halide perovskites. Here, the progress of PSCs is reported following a detailed description on the discovery of PSCs. The first solid-state PSCs were based on sensitization concept using a sub-micrometer mesoporous TiO_2 film whose surface was coated with nano-sized methylammonium lead iodide ($MAPbI_3$), which had evolved to n-i-p and p-i-n planar device structures. Recent high efficiencies were mostly demonstrated using formamidinium lead iodide ($FAPbI_3$) perovskite. To increase further the PCE to more than 30%, the current density should approach 28 mA/cm^2 and fill factor 90% while keeping the voltage near 1.2 V using a perovskite with bandgap less than ~1.47 eV (theoretical current density = 29.4 mA/cm^2). Thus, a strategy should be well established to make a defect-minimized perovskite film and the interface-engineered PSCs as well. Finally, effective methodology for improving stability of PSCs is discussed.

Keywords Perovskites · Photovoltaic · Additives · Crystallization · Passivation · Stability

Introduction

Since the seminal work on solid-state PSCs reported in 2012 by Park's research group [1], halide perovskite materials and PSCs received great attention due to unconventional semiconducting properties and unprecedented light-to-electricity conversion characteristics. As a result, a certified PCE of 26.1% was achieved as of March 2024 [2], which is comparable to the PCE of a single junction silicon solar cell. The highest PCE of 33.9% was achieved by putting a PSC on top of the Si cell to construct a perovskite/Si tandem solar cell [2]. This indicates that PSCs are promising technology in the field of photovoltaics and expected to play a central role in photovoltaic market in near future.

In this report, discovery of the solid-state PSC is described, followed by recent progresses of PSCs. A brief introduction of halide perovskite structure and basic optoelectronic properties is described. Methodologies for improving efficiency and stability of PSCs are investigated. In addition, current issues for commercialization are discussed.

Discovery of Solid-State Perovskite Solar Cell

Perovskite is crystal structure with chemical formula of ABX_3, where A-site cation is occupied in cubo-octahedral space by coordinating 12 X anions and B-site cation is stabilized in octahedral site by coordinating 6 X anions [3–5]. Figure 1a shows a schematic illustration of unit cell of perovskite. X can be oxygen, sulfur and halide, called sometimes oxide perovskite, chalcogenide perovskite and halide perovskite, respectively. Depending on the oxidation state of anions, oxidation states of A and B cations are determined. For instance, oxide perovskites can exhibit combinations of (A, B) oxidation states such as (1+, 5+), (2+, 4+), or (3+, 3+). For divalent anions, variety of elements can be A and B sites due to variety of oxidation state combinations.

✉ Nam-Gyu Park
  npark@skku.edu

1 School of Chemical Engineering and Center for Antibonding Regulated Crystals, Sungkyunkwan University, Suwon 16419, Republic of Korea

2 SKKU Institute of Energy Science and Technology (SIEST), Sungkyunkwan University, Suwon 16419, Republic of Korea
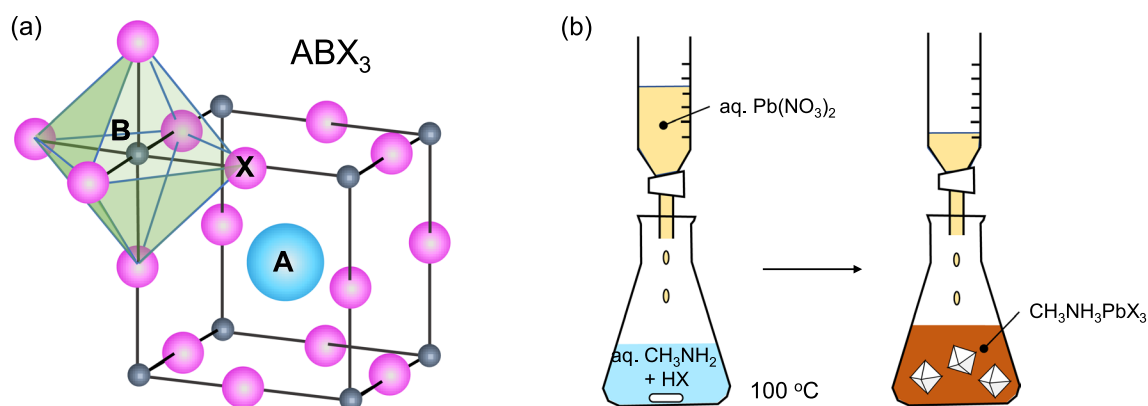
Fig. 1 **a** Structure of perovskite with chemical formula of ABX$_3$. For PSCs, methylammonium or formamidinium cation is commonly used for A site ion and divalent lead or tin can be used for B site cation and X is halide anion. Reproduced with permission from Ref. [3], Copy-right 2014, Elsevier Ltd. **b** Aqueous synthesis of MAPbX$_3$ perovskite crystals by addition of aqueous Pb(NO$_3$)$_2$ in aqueous CH3NH$_2$/HX solution at 100 °C. The experimental setup was reorganized based on Ref. [6]

However, for monovalent anion such as halide, (A, B) oxidation state will be only (1+, 2+). The (2+, 1+) combination might be possible but rare because coordination number-related space should be taken into account when selecting cations.

Organic ammonium cation was first introduced in halide perovskites in 1978 [6]. Methylammonium lead trihalides (MAPbX$_3$) were synthesized in aqueous solution at 100 °C, where aqueous Pb(NO$_3$)$_2$ solution was slowly added into the hot aqueous solution containing methylamine and hydro halide, which led to the crystal precipitation (Fig. 1b). This crystal growth at high temperature was unusual and no explanation was given. In 2015, high temperature crystal growth of MAPbI$_3$ was first reproduced by Hagfeldt group, where MAPbI$_3$ crystals were grown in a polar aprotic solvent γ-butyrolactone at 190 °C via inverse solubility [7]. This technology was further advanced and called "inverse temperature crystallization" [8]. The color of the products changed from colorless to black going from chloride to iodide. This indicates that optical bandgap is decreased with increasing halide ionic size from chloride to iodide. In the report [6], molecular motion of methylammonium cation in cubo-octahedral site was speculated to satisfy the Goldschmidt tolerance factor based on spherical ions [9] because non-spherical methylammonium ion could be a spherical shape by rotation. This assumption was proved by the quasielastic neutron scattering measurements in 2015 [10].

Report on the synthesis of MAPbX$_3$ perovskites in 1978 induced further research on their phase transition [11] and thermodynamic properties [12]. However, there was no reports on perovskite photovoltaics until the conference report on the perovskite-sensitized solar cell presented by Miyasaka at Nanoeuro 2007 in St. Gallen, Switzerland in 2007. Sensitization of halide perovskite MAPbI$_3$

nanocrystal on a mesoporous 8–10 µm-thick TiO$_2$ film generated a power conversion efficiency of 3.8% [13], where a polar liquid electrolyte (0.15 M LiI and 0.075 M I$_2$ dissolved in methoxyacetonitrile) was still employed. Since halide perovskite tends to be dissolved in the presence of polar liquid electrolyte, the perovskite-sensitized solar cell with acetonitrile-based liquid electrolyte is quite unstable because of dissolution of the perovskite in polar solvent (polarity of acetonitrile is 11.8). Less polar solvent is thus expected to improve stability of perovskite. Park's group modified electrolyte using a less polar solvent of ethyl acetate (polarity is 8.6), which was applied to a MAPbI$_3$-sensitized solar cell and demonstrated higher PCE of 6.5% [14]. In addition, a reproducible recipe to prepare the perovskite precursor solution was provided in ref. 14, where the perovskite was reproducibly formed using a high concentration (40%) precursor solution based on the study of dependence of external quantum efficiency (EQE) on the precursor concentration ranging from 10 to 40%. Nevertheless, the less polar ethyl acetate-based electrolyte was not enough to protect dissolution of perovskite. This means that halide perovskite cannot be used as a light absorber in the presence of polar liquid electrolyte. To solve this problem, two methods have been considered: one is wrapping the perovskite with hydrophobic materials and the other is replacing the liquid electrolyte with solid hole conducting materials (HTMs). The first idea was not successful because of poor contact with electrolyte due to the presence of hydrophobic yet insulating barrier between electrolyte and perovskite. The second idea of using a HTM instead of liquid electrolyte was indeed successful. Since we used a mesoporous TiO$_2$ film whose surface was covered by the perovskite nanocrystals, molecular type HTM was better than polymeric HTM in terms of infiltration of HTM in the randomly connected mesopores.

Spiro-MeOTAD (often, spiro-OMeTAD) molecular HTM was confirmed to be successfully infiltrated into the mesoporous TiO_2 film, where the submicrometer-thick TiO_2 film was sufficient because of high absorption coefficient of $MAPbI_3$ exceeding 10^4 cm^{-1} [14]. A PCE of 9.7% was achieved from the spiro-MeOTAD/$MAPbI_3$ junction at 600 nm-thick TiO_2 film, where stability with unencapsulated device was shown for 500 h [1]. To understand change separation mechanism of the solid-state PSCs, femtosecond transient absorption study was performed. Interestingly, the same bleaching at 480 nm and positive peak at around 640 nm were observed for both Al_2O_3 and TiO_2 (Fig. 2a and b). When considering that the conduction band position of Al_2O_3 is higher than that of $MAPbI_3$, the similar spectral response for the TiO_2/$MAPbI_3$ junction indicates that electron injection from perovskite to TiO_2 is hard to occur. On the other hands, the excited state of $MAPbI_3$ is rapidly quenched in the presence of spiro-MeOTAD HTM (Fig. 2c and d), which indicates that hole is separated quickly by spiro-MeOTAD. Based on the transient absorption study, excited electrons in $MAPbI_3$ are likely to be transported through the thin layer of $MAPbI_3$ on the TiO_2 surface, which might be formed during spin-coating and hard to be detected by electron microscopy, and holes are injected to spiro-MeOTAD. This charge separation mechanism in the scaffold-oxide-based solid-state PSCs was clearly observed by FTO/Al_2O_3/$MAPbI_3$/spiro-MeOTAD device configuration [15].

The seminal report on the stable solid-state PSCs triggered perovskite photovoltaic research, which indeed leads to a certified PCE over 26% [16], where maximum short-circuit photocurrent density (J_{sc}), open-circuit voltage (V_{oc}) and fill factor (FF) was 26.13 mA/cm^2, 1.201 V and 85.2%, respectively. This achievement surpasses the PCEs of CIGS (23.6%) and CdTe (22.4%) solar cells and is comparable to the PCE of crystalline Si solar cells (26.0–26.7% depending on p- or n-type characteristics and device structures). In Fig. 3, the EQE spectra and J–V curves for the record efficiency PSCs are shown depending on aperture area (26.1% from 0.05 cm^2 and 25.2% from 1.03 cm^2) are presented. It is worth noting that EQE remains above 90% across almost the entire wavelength ranging from 400 to 800 nm.

Methodologies that Contributed to the Improvement of Efficiencies

PSCs can be made by either n-i-p or p-i-n structures, where the p-i-n structure is also called an inverted PSC. As can be seen in Fig. 4a, electron transporting layer (ETL) is deposited on a transparent conducting oxide (TCO) substrate, such as fluorine-doped tin oxide (FTO), to make the n-i-p PSCs, where hole transporting layer (HTL) like spiro-MeOTAD is required on top of the perovskite film. For constructing the p-i-n PSCs in Fig. 4b, a HTL is first placed on a TCO substrate and a PCBM/C_{60} layer can be used as an ETL, where PCBM (phenyl-C61-butyric acid methyl ester) is C_{60}
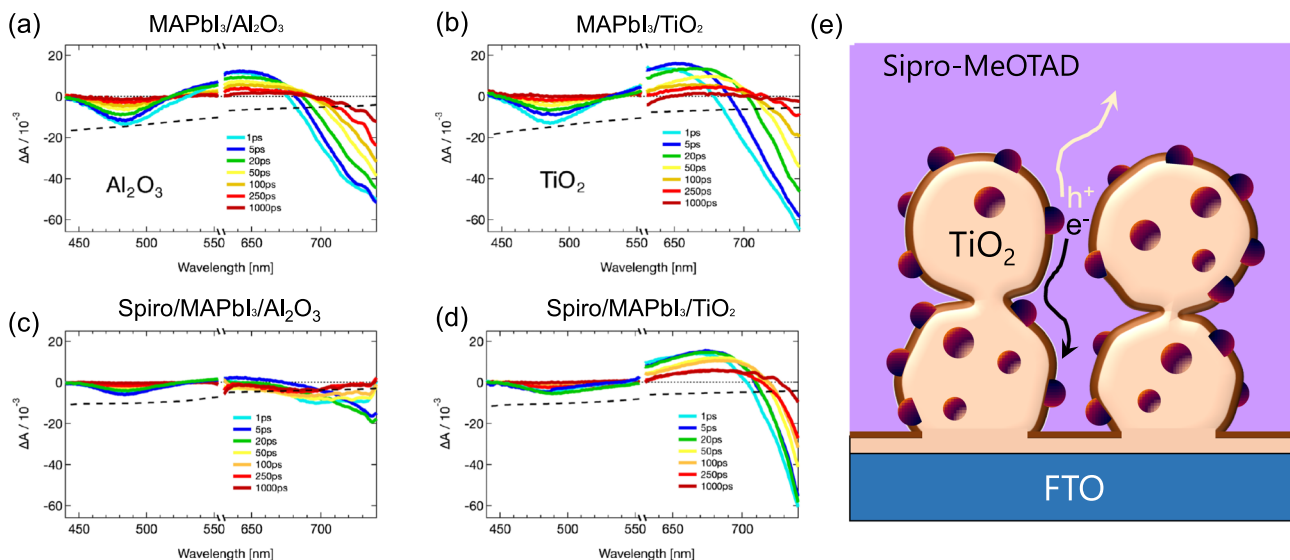

Fig. 2 Femtosecond transient absorbance spectra obtained by using pulsed excitation at 580 nm and white light continuum probe for **a** $MAPbI_3$/Al_2O_3, **b** $MAPbI_3$/TiO_2, **c** Spiro-MeOTAD/$MAPbI_3$/Al_2O_3, and **d** Spiro-MeOTAD/$MAPbI_3$/TiO_2, recorded at various time delays after excitation (color lines). Black dashed lines represent the absorbance spectrum of the sample. Reproduced with permission from Ref. [1], Copyright 2012, Springer Nature. **e** Schematic illustration of charge separation mechanism based on the femtosecond transient absorption results in **a–d**
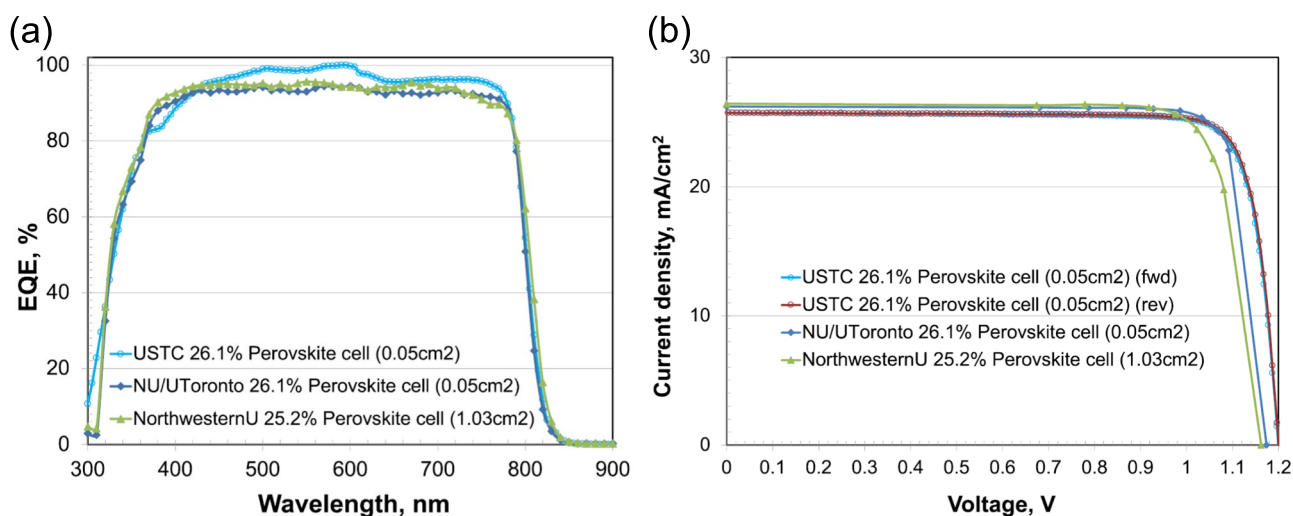
Fig. 3 a EQE for the record efficiency PSCs depending on aperture area. **b** Corresponding current density–voltage (*JV*) curves (fwd and rev stand for forward and reverse scan, respectively). USTC and NU represent University of Science and Technology of China and Northwestern University, respectively. Reproduced with permission from Ref. [16], Copyright 2024, John Wiley & Sons Ltd

Fig. 4 PSCs with (a) n-i-p and (b) p-i-n structure. BCP is bathocuproine and used as a buffer layer in the p-i-n PSCs
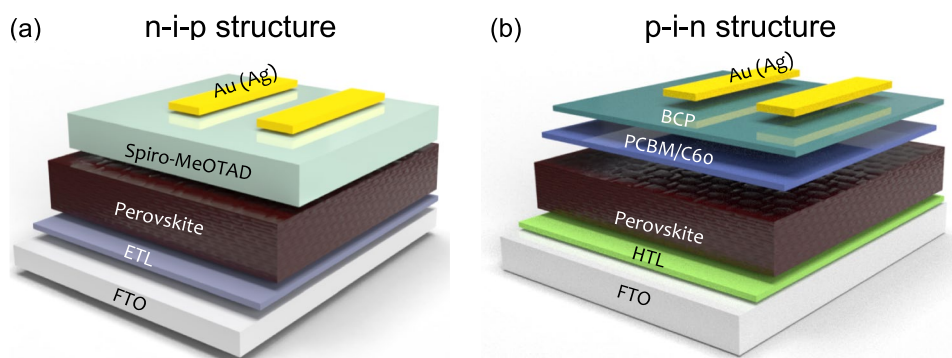
derivative. Except for spiro-MeOTAD and PCBM/C_{60}, various materials were studied for ETL and HTL [5, 17–20]. It is recommended to prepare highly transparent ETL or HTL in the n-i-p or the p-i-n PSCs for the perovskite layer to absorb the incoming light without absorption by HTL and ETL.

Defect-less high-quality perovskite film is prerequisite for high efficiency. Spin-coating method is frequently used to deposit the perovskite film. However, a rapid evaporation of the solvent during the spin-coating leads to a fast crystallization of perovskite film, which indeed results in small grains with poor crystallinity. To improve crystallinity with large grains, kinetic control is necessarily required via intermediate formation. Since a perovskite precursor solution contains polar aprotic solvents, commonly dimethyl sulfoxide (DMSO) and dimethyl formamide (DMF) because PbI_2 and MAI for $MAPbI_3$ can be dissolved in such the polar aprotic solvents. DMSO and DMF can act as Lewis base because of lone pairs on oxygen atom, where basicity is higher for DMSO (donor number (DN) = 26.5) than

DMF (DN = 22.4) [21], and PbI_2 acts as Lewis acid (Fig. 5a). Interaction between Lewis acid and base leads to an adduct because of further stabilized lone pair in molecular orbital of the adduct (Fig. 5b). Selective removal of the DMF solvent by dripping diethyl ether while spinning was found to form a colorless MAI·PbI_2·DMSO adduct intermediate as shown in Fig. 5c, where DMSO can be controlled by mild heating due to rather weak chemical interaction with Lewis acids. Two-step heating can remove DMSO from the intermediate and thereby form a high quality $MAPbI_3$ [22]. The adduct-process eventually contributed significantly to improving PCE of PSCs.

Another approach is composition engineering. $MAPbI_3$ for the first solid-state PSCs has a bandgap of about 1.55 eV, which means that the minimum light energy to excite electrons from the valence band of $MAPbI_3$ required wavelength of about 800 nm (1240/1.55 = 800). Replacing MA^+ with FA^+ lowers band gap to about 1.47 eV. Thus, $FAPbI_3$-based PSCs might achieve higher PCE due to more
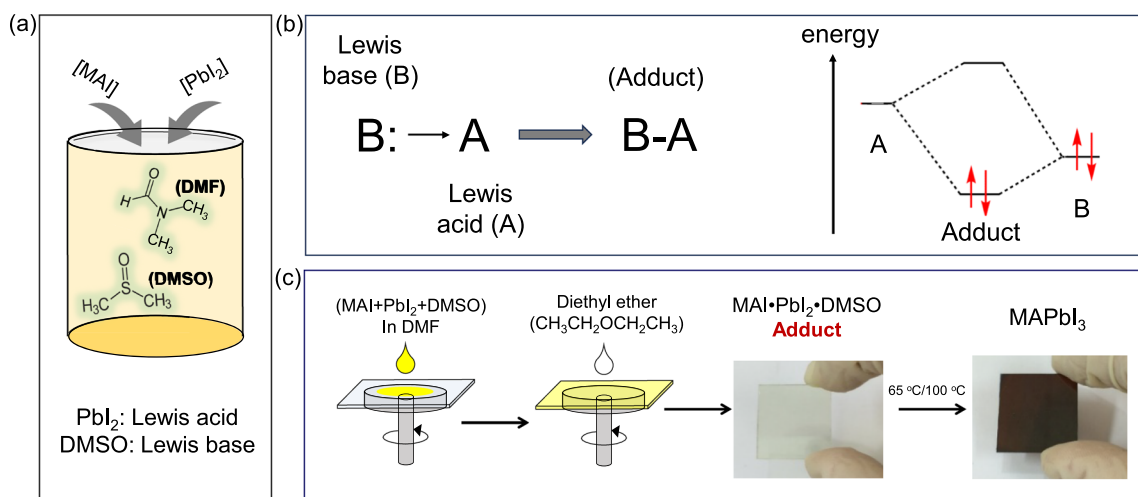
Fig. 5 a Precursor solution made by dissolving MAI and PbI$_2$ in DMSO and DMF. DMF was used as a solvent and DMSO was used as a Lewis base. **b** Adduct formation by reacting Lewis base with Lewis acid. Adduct further stabilizes lone pair of the Lewis base. **c** Selective removal of DMF by diethyl ether to form a MAI·PbI$_2$·DMSO adduct. High-quality MAPbI$_3$ perovskite film was fabricated via two-step heating. Reproduced with permission from Ref. [21]. Copyright 2015. American Chemical Society

J_{sc} than MAPbI$_3$ because of extension of light absorption up to 843 nm. In Fig. 6a and b, calculated XRD patterns are depicted for MAPbI$_3$ and FAPbI$_3$ at 298 K. FAPbI$_3$ is known to phase transformation from high-temperature-stabilized α phase (black color, perovskite structure) to low-temperature-stabilized δ phase (yellow color, non-perovskite structure) as shown in Fig. 6c. It was observed that

δ-FAPbI$_3$ could be rapidly converted to α-FAPbI$_3$ at 185 °C within 2 min, while α-to-δ phase transition took 10 days at room temperature [23]. This indicates that α-FAPbI$_3$ is unstable at room temperature, which might be due to large cation size of FA$^+$ compared to MA$^+$. To stabilize α-FAPbI$_3$ even at room temperature, introduction of smaller cation in FA$^+$ site is required. We eventually solved this problem
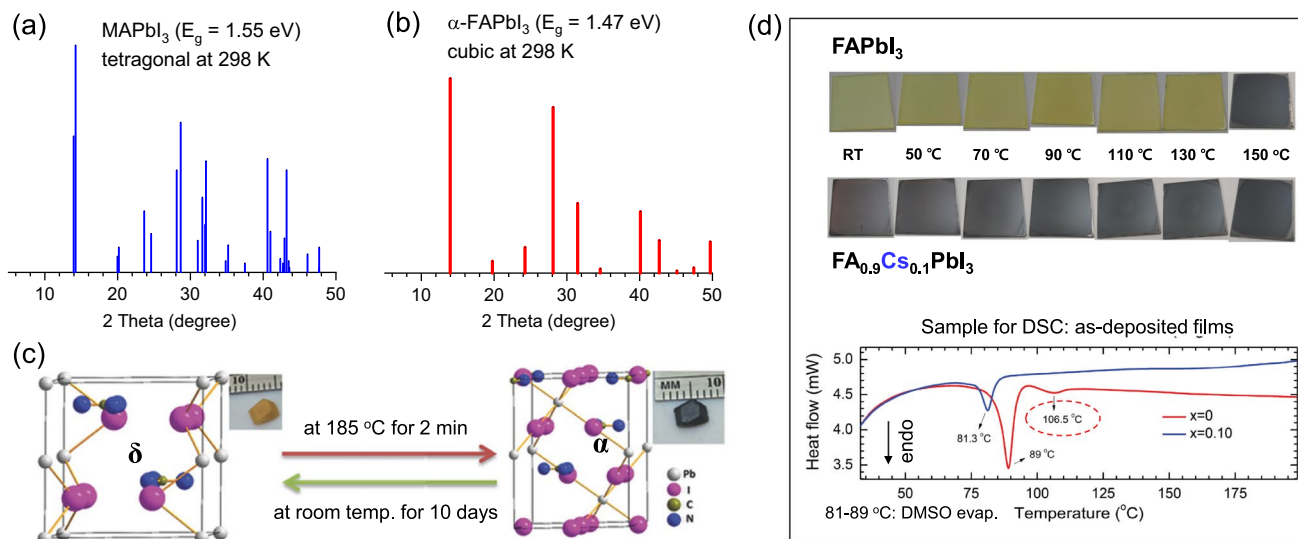

Fig. 6 Calculated XRD patterns of **a** MAPbI$_3$ and **b** FAPbI$_3$. **c** Phase transition between yellow δ-phase FAPbI$_3$ and black α-phase FAPbI$_3$. Reproduced with permission from Ref. [23]. Copyright 2016. John Wiley & Sons Ltd. **d** Photographs of FAPbI$_3$ and FA$_{0.9}$Cs0.1PbI$_3$ films depending on annealing temperature and DSC data of as-deposited FAPbI$_3$ and FA$_{0.9}$Cs$_{0.1}$PbI$_3$ films. Endothermic peaks at around 81–89 °C are related to evaporation of DMSO. Endothermic peak at 106.5 °C for FAPbI$_3$ is due to δ-to-α phase transition, while no peak corresponding to phase transition was observed for FA$_{0.9}$Cs$_{0.1}$PbI$_3$. Reproduced with permission from Ref. [24]. Copyright 2015. John Wiley & Sons Ltd

by replacing 10% of FA cation with Cs cation, leading to a nominal composition of $FA_{0.9}Cs_{0.1}PbI_3$ [24]. Figure 6d shows that 10 mol% Cs incorporation is sufficient to stabilize α phase at low temperature without requiring energy for δ-to-α transition as confirmed by differential scanning calorimetry (DSC) measurement. Thus, Cs cation acts as a kind of stabilizer. This work triggered research on multiple cation PSCs [25–30]. Adduct intermediate process and composition engineering have indeed contributed to improving efficiency of PSCs.

Future Research Directions for Improving Efficiencies

Strategies for Improving Efficiency

In Fig. 7, PCEs of PSCs are displayed with respect to band gap (E_g) of the corresponding perovskite compositions of $MAPbI_3$, $(Rb/Cs/MA)_{1-x}FA_xPb(I_{0.84}Br_{0.16})_3$ ($0.75 < x < 0.8$), $MA_{1-x}FA_xPb[I_y(Br/HCOO)_{1-y}]_3$ ($0.95 \leq x$, $y \leq 1$), and $(MDA/Cs)_{1-x}FA_xPbI_3$ ($0.96 < x \leq 0.97$), where MDA represents methylenediammonium cation (MDA^{2+}) [31]. The data were based on the best achievement up to 2022. The composition of $MA_{1-x}FA_xPb[I_y(Br/HCOO)_{1-y}]_3$ ($0.95 \leq x$, $y \leq 1$) is symbolized with green circle and $(MDA/Cs)_{1-x}FA_xPbI_3$ ($0.96 < x \leq 0.97$) with red triangle in Fig. 7. It is worth to note that overall efficiency might not depend on E_g because similar PCEs of 25% were obtained with E_g from 1.47 to 1.56 eV, which corresponds to 80% of S–Q limit (see Fig. 7a). However, when investigating photovoltaic parameters more in detail (Fig. 7b–d), the pure

iodide system of $(MDA/Cs)_{1-x}FA_xPbI_3$ shows a gap in J_{sc} between the observed values and the S–Q limit (Fig. 7b), while there is a gap in V_{oc} for the mixed halide composition of $MA_{1-x}FA_xPb[I_y(Br/HCOO)_{1-y}]_3$ (Fig. 7c). This underlines that pure iodide composition with smaller E_g needs to increase J_{sc} further, whereas further increase in V_{oc} is required for the mixed halide composition with relatively larger E_g. This also indicates that effective trap density might be dependent on perovskite composition when considering trap density–V_{oc} relation. Thus, research direction toward higher PCE seems to be different depending on perovskite composition.

Facet-Dependent Photocurrent

As aforementioned strategy for improving further PCE by increasing J_{sc} or V_{oc} depending on perovskite composition, we have been interested in methodologies to increase J_{sc} of pure iodide system such as $FA_{1-x}Cs_xPbI_3$. While exploring an effective method, we are motivated by the report on inhomogeneity of photocurrent on the perovskite surface measured by atomic force microscopy (AFM) under illumination [32], where this inhomogeneity was speculated to be related to crystal facet. However, the facets could not be distinguished from the perovskite film surface [32]. Thus, we wanted to prepare a perovskite film showing clear facets, which was realized via additive engineering [33]. In Fig. 8, compared with scanning electron microscopy (SEM) image of the perovskite film prepared by a conventional precursor solution containing $FAPbI_3$ and MACl (Fig. 8a), the addition of piperidine additive into the precursor solution significantly changes perovskite film morphology showing clearly
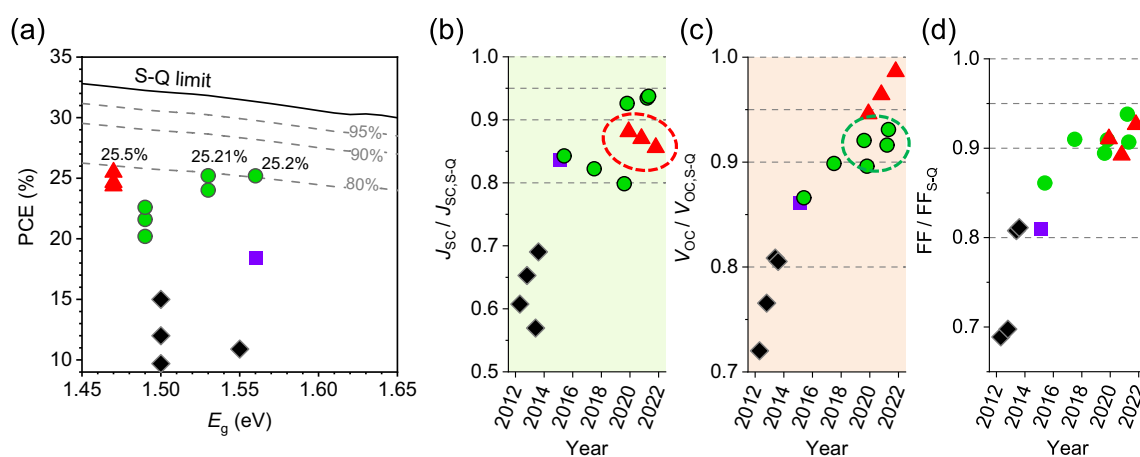

Fig. 7 **a** PCEs of PSCs with respect to band gap (E_g), along with Shockley–Queisser (S–Q) limit. The black diamond represents a perovskite composition with $MAPbI_3$, purple square $(Rb/Cs/MA)_{1-x}FA_xPb(I_{0.84}Br_{0.16})_3$ ($0.75 < x < 0.8$), green circle $MA_{1-x}FA_xPb[I_y(Br/HCOO)_{1-y}]_3$ ($0.95 \leq x$, $y \leq 1$), and red triangle $(MDA/Cs)_{1-x}FA_xPbI_3$ ($0.96 < x \leq 0.97$). Normalized photovoltaic parameters of **b** J_{sc}, **c** V_{oc} and **d** FF observed from the record PSCs with respect to the corresponding E_g-dependent theoretical S–Q limit. Reproduced with permission from Ref. [31]. Copyright 2023. John Wiley & Sons Ltd
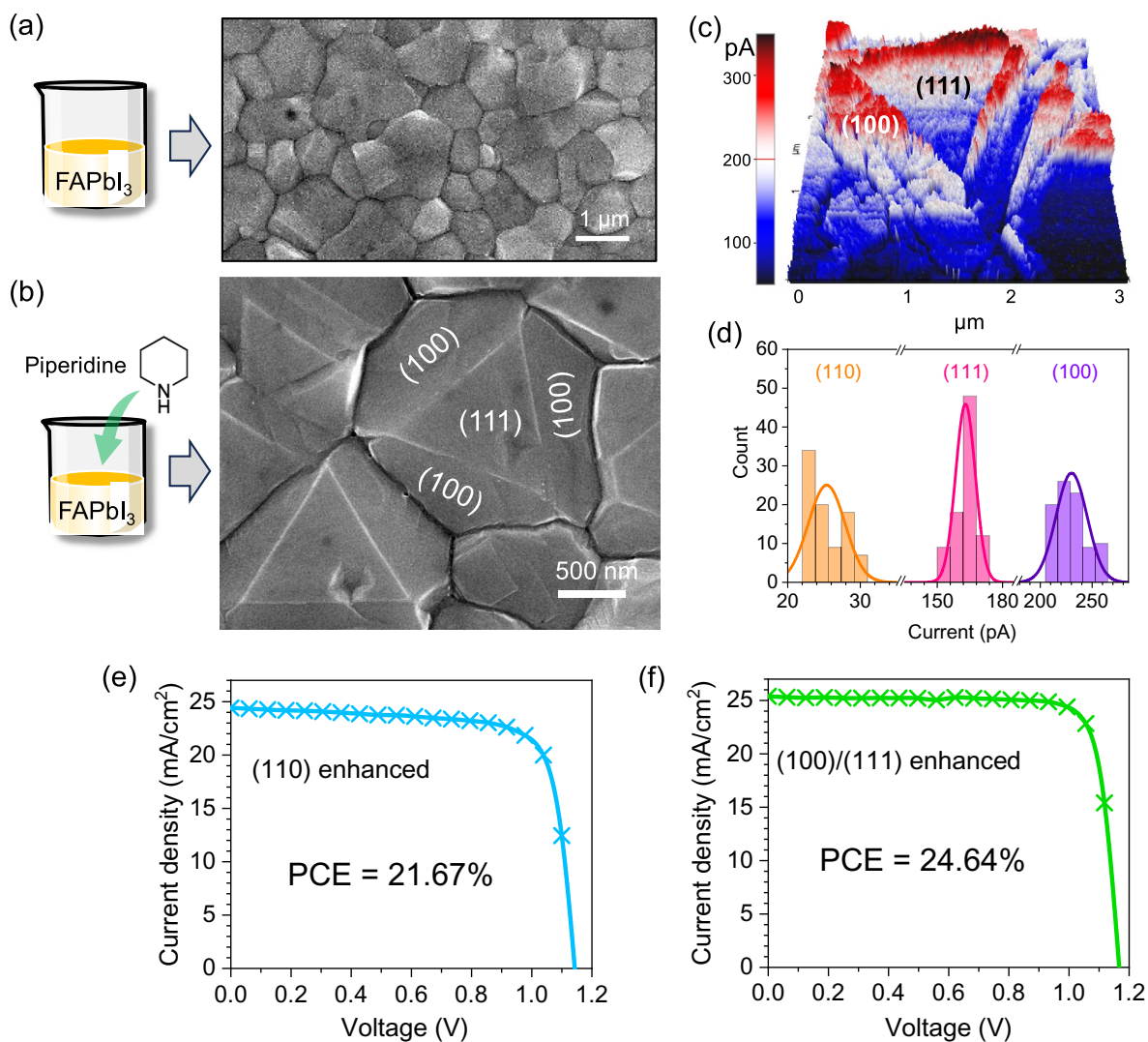
Fig. 8 SEM images of FAPbI$_3$ (small amount of Cs was incorporated) perovskite film prepared by the precursor solution **a** without and **b** with piperidine additive. **c** Photocurrent-AFM images under illumination and **d** corresponding current output depending on (100), (111) and (110) crystal facets. *J–V* curves of best performing PSCs based on **e** (110) enhanced film and **f** (100)/(110) enhanced film. Reproduced with permission from Ref. [33]. Copyright 2022. Elsevier Inc

(100) and (111) crystal facets (Fig. 8b). With the perovskite film having the (100) and (111) facets, surface photocurrent was investigated using AFM under illumination (Fig. 8c). Interestingly, the (100) facet showed highest photocurrent of about 230 pA and a little bit lower, yet comparable photocurrent (~ 170 pA) was observed from the (111) facet (Fig. 8d). On the other hand, the perovskite surface dominated with (110) facet exhibited extremely poor photocurrent (~ 26 pA). This clearly demonstrated facet-dependent photocurrent, which was explained by the exciton generation rate [33]. As expected, the (100)/(111) enhanced perovskite film showed much higher PCE than the (110) enhanced one (Fig. 8e and f). This work can give an important insight into perovskite film design for high PCE.

Homogenizing Cations in the Perovskite Films

In order to improve J_{sc} via enhancing charge extraction capability, well-matched band alignment is required. As aforementioned, a small amount of Cs cation is required to stabilize α phase FAPbI$_3$. In this case, phase purity in the entire FA$_{1-x}$Cs$_x$PbI$_3$ film is highly required. However, FA and Cs cations might not be homogeneously distributed across the perovskite film. Time-of-flight secondary-ion mass spectroscopy (ToF–SIMS) measurements reveal that the perovskite film prepared by the conventional precursor solution showed inhomogeneous out-of-plane cation distribution [34], where FA-rich composition was formed on the top surface whereas Cs-rich composition was made on the bottom of the film

(Fig. 9a). Such an inhomogeneous cation distribution across the film might be due to difference in crystallization and phase transition kinetics to form perovskite phase with FA and Cs cation. Moreover, charge transport is affected by the inhomogeneity because of difference in band positions between FAPbI$_3$ and CsPbI$_3$, which can have ill influence on photovoltaic performance. 1-(Phenylsulfonyl)pyrrole (PSP) was synthesized to use as an additive for controlling kinetics (Fig. 9b). Thanks to the similar dimension between molecular PSP and I–Pb–I and the chemical interaction between PSP with δ^+–δ^-–δ^+ (δ^- for sulfonyl group and δ^+ for phenyl and pyrrole group) and I–Pb–I, PSP successfully controlled crystallization and phase transition kinetics. This eventually homogenized FA and Ca cations in the entire film, leading to carrier extraction equilibrium and higher PCE exceeding 26%.

Future research Directions for Improving Stability

Facet-Dependent Moisture Stability

3D halide perovskite is known to be unstable under moisture environment. However, the origin of such a moisture instability has not been well understood. Besides ionic nature of halide perovskite, we have been motivated to investigate facet-dependent moisture stability since water adsorption might be expected to depend on facets due to different surface charge and energy. As shown in Fig. 10a, the (100)/(111) enhanced perovskite film, prepared by the

aforementioned piperidine additive [33], was exposed to 40% relative humidity (RH) for 200 h, from which the (100) facet was found to be seriously degraded, whereas the (111) facet was quite stable [35]. Based on the confocal PL measurement for the 200 h-exposed film (Fig. 10b), PL emission was observed from the (111) facet, while no PL emission was detected on the (100) facet. This indicates that the moisture turned the (100) facet a non-perovskite phase. To further validate the changes after exposure, photocurrent-AFM was measured. The degraded (100) facet by moisture could not generate photocurrent and the degraded (100) facet was confirmed to be non-perovskite δ phase (Fig. 10c), accompanied by change in the layer height due to the phase change. On the other hand, no change in both photocurrent and height was observed for the (111) facet (Fig. 10d). This confirms again that (111) facet is moisture tolerant. Since we discovered the facet-dependent moisture stability and moisture-tolerant (111) facet, the (111)-dominated perovskite film was expected to improve moisture stability. For this purpose, cyclohexylamine with two hydrogens was selected to use as an additive (Fig. 10e), which led to 85–98% of the (111) facets based on the exposed-area percentage calculation (Fig. 10f). As expected, the (111)-dominant film-based PSCs without encapsulation was more stable than the PSCs based on the (100)/(111) mixed facet under 30–40% RH condition (Fig. 10g). Since efficiency and stability were found to be strongly dependent on crystal facet, facet engineering is important research topic toward stable and higher efficiency PSCs [33]. In addition to the moisture stability, phase stability of especially FAPbI$_3$ is of critical
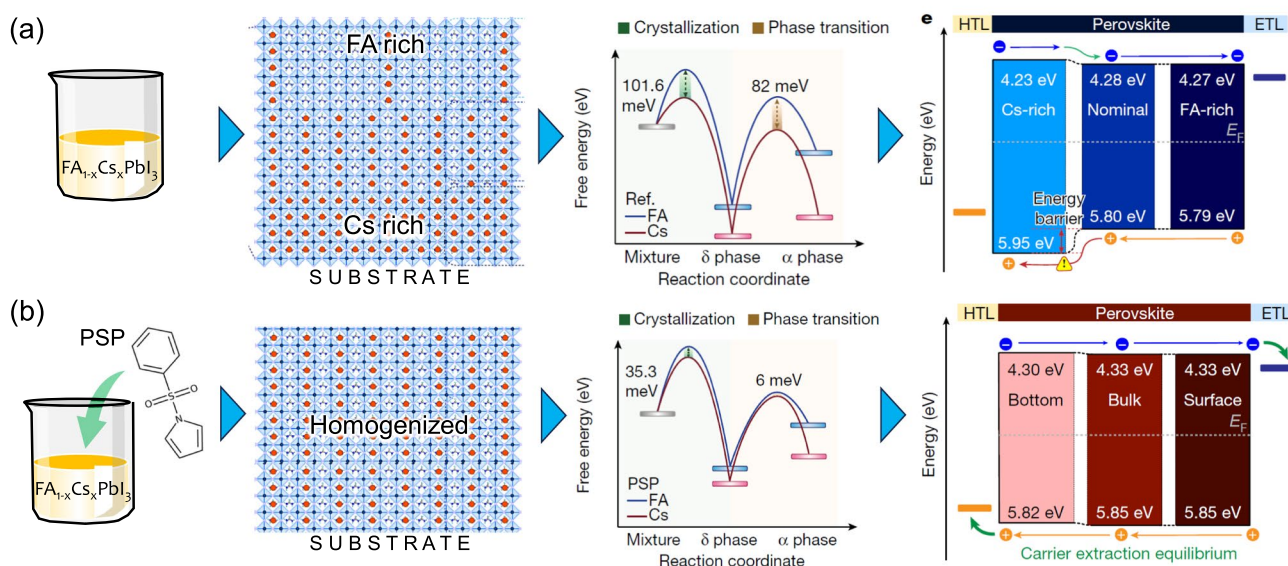

Fig. 9 Schematic cation distribution, Free energy changes, and band structure of FA$_{0.95}$Cs$_{0.05}$PbI$_3$ film prepared by precursor solution **a** without and **b** with PSP. Reproduced with permission from Ref. [34]. Copyright 2023. Springer Nature
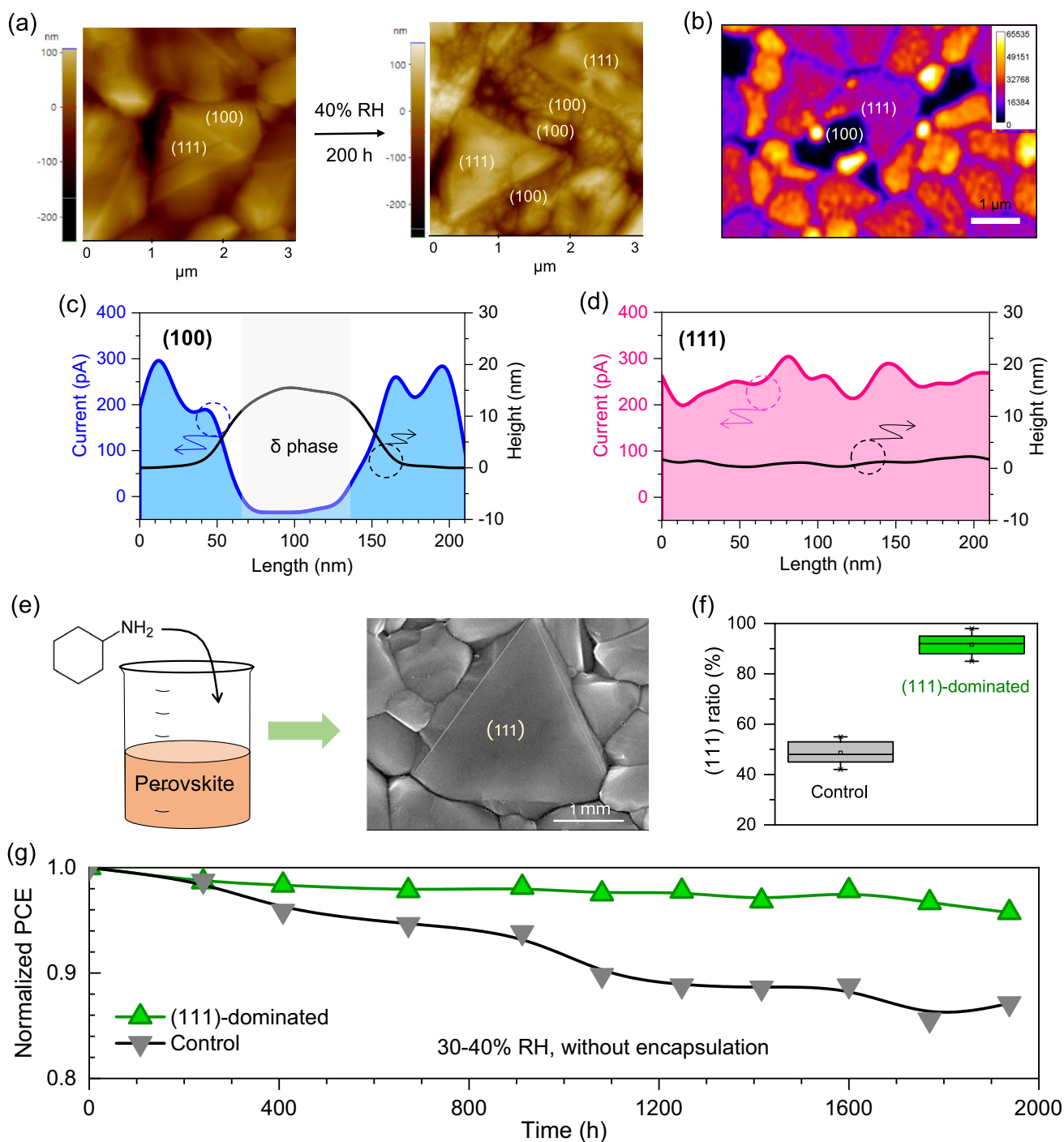
Fig. 10 **a** AFM images of (100) and (111) enhanced perovskite films before and after exposure to 40% RH for 200 h. **b** 2D PL image of the exposed film under 40% RH for 72 h. Surface photocurrent and height of the 40% RH-aged perovskite films for **c** the (100) and **d** the (111) facet. The aging time at 40% RH was 72 h. **e** SEM image of the perovskite film prepared by cyclohexylamine additive, resulting in **f** (111)-dominated film composed of ca. 98% of (111) facet. **g** Long-term stability test with PSCs without encapsulation under 30–40% RH. Reproduced with permission from Ref. [35]. Copyright 2023. American Association for the Advancement of Science

in achieving the stable PSCs. Regarding phase stability of the perovskite layer, kinetic and thermodynamic stability of FAPbI$_3$ is involved, which should be carefully investigated, well understood and managed by specific methodologies [31, 36, 37].

Interface Engineering for Improving Operational Stability

The weak adhesion can exist at the charge transport layer (CTL)/perovskite interface due to the composition inhomogeneity and the strain in the perovskite layer [38–40]. This inhomogeneity might cause a weak homojunction of perovskite adjacent to the CTLs [41]. Since there is possibility of workfunction (W_F) difference at the perovskite homojunction with weak adhesion and thus the weak adhesion interface can have ill influence on stability, regulating W_F is required to improve the stability. It is then questioned how we determine W_F of the weak homojunction of perovskite layer near the CTL. For the n-i-p structure with a SnO$_2$ CTL, peeling off the perovskite layer from the SnO$_2$-coated FTO substrate might be a reasonable method to determine the W_F of the weak adhesion homojunction. Figure 11a shows a peeling off the perovskite layer from the SnO$_2$-coated FTO substrate, where the perovskite could not be completely peeled off from the SnO$_2$ layer, instead, a thin perovskite layer was still adhered on the SnO$_2$ layer [42]. The surface on the bottom of the perovskite film and the upper surface

of the SnO$_2$ film were labeled "surface A" and "surface B," respectively. W_F of the surface A and the surface B was determined to be 4.23 eV and 3.88 eV, respectively, using Kelvin probe force microscope (KPFM) (Fig. 11b). The difference in W_F is indicative of existence of homojunction. Ultraviolet photoelectron spectroscopy (UPS) in Fig. 11c shows a similar ΔW_F observed by the KPFM measurements. W_F of the surface A shifted further to 4.47 eV after photovoltaic operation for 50 h (Fig. 11b), which might be due to decomposition and/or change in structural phase of perovskite at the weak homojunction under illumination.

To solve the problem of the change in W_F after operation, a siloxane-based self-assembled molecule (SAM) was introduced in between the SnO$_2$ layer and the perovskite layer, where one should carefully consider the functionality of the terminal group. We selected electron-withdrawing nitrile group to passivate the defect, mostly iodide vacancy, at the bottom of the perovskite and enhance the adhesion of the buried interface (Fig. 11d). Compared with other electron-withdrawing group, like Cl, Br and I, at the terminal position of silane derivatives, density functional theory (DFT) calculation revealed
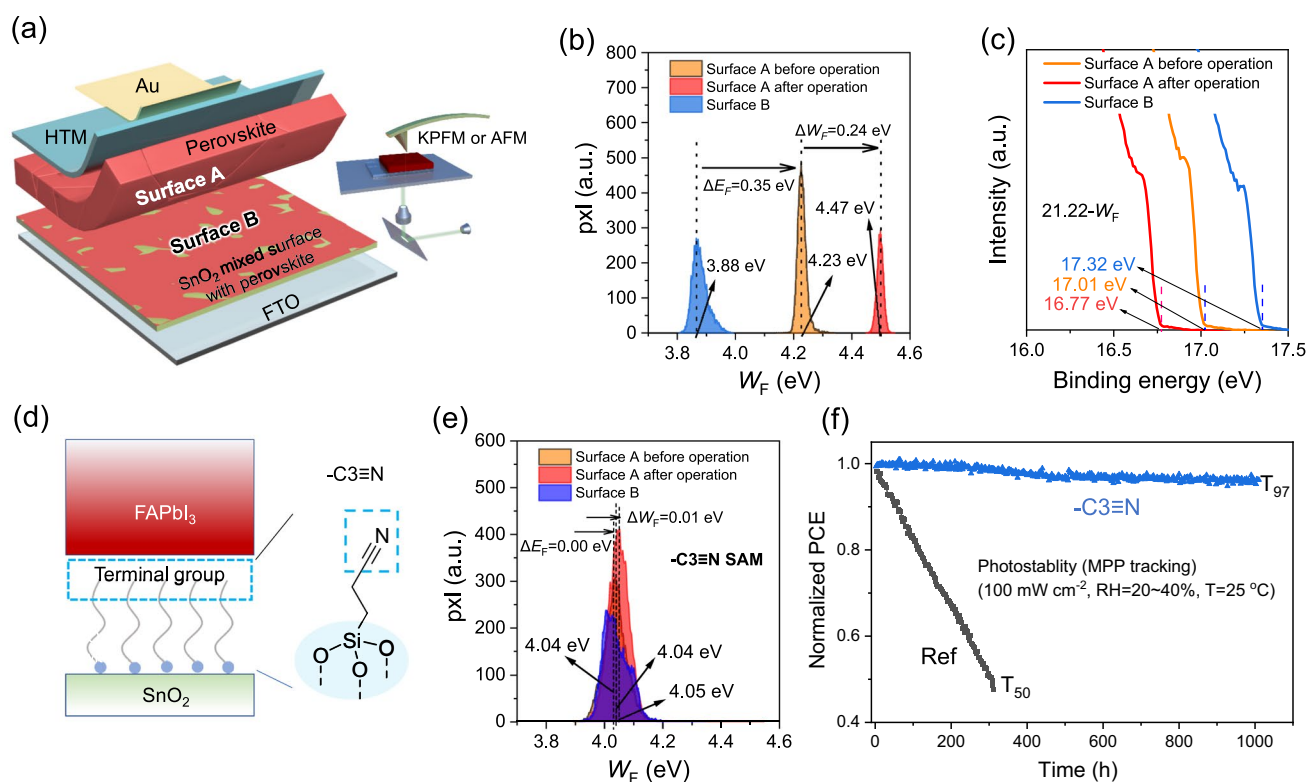

Fig. 11 **a** Schematic diagram of peeling off the buried interface of the n-i-p PSCs. Inset shows the KPFM or AFM probe for measuring the W_Fs of surface A and surface B. **b** W_F distribution of surface A before and after the operation and surface B, estimated from KPFM. Pxl in *y* axis represents pixel. **c** Secondary cutoff region of UPS for surface A before and after the operation and surface B. **d** Schematic diagram showing the surface treated SnO$_2$ with 3-(triehtoxysilyl)propionitrile (–C3≡N). (e) W_F distribution of surface A before and after the operation and surface B. The SnO$_2$ surface was treated with–C3≡N. **f** MPPT under continuous one sun illumination for the encapsulated PSCs without (Ref) and with with–C3≡N. Reproduced with permission from Ref. [42]. Copyright 2024. Elsevier Inc

that interface adhesion energy was higher for the nitrile group than for the halogen group. KPFM measurement in Fig. 11e showed a negligible difference in ΔW_F before and after operation for the SAM-modified sample due to the energy-level alignment by the introduction of the SAM. As a result, photostability of PSCs was significantly improved as shown in Fig. 11f, demonstrating 97% of the initial PCE was maintained after 1000 h-maximum-power-point-tracking (MPPT).

Conclusions and Perspectives

In this review, the historical background of the solid-state perovskite solar cell discovery was described in detail. The significant improvement in PCE of PSCs from 9.7 to 26.1% were realized thanks to the three major contributions. The Lewis acid–base adduct approach contributed to preparing high quality perovskite films. Additives in the perovskite precursor solutions played important role in controlling crystallization kinetics and grain size, which contributed to reduction of bulk and grain boundary defects. Interface engineering contributed equally to improving photovoltaic performance. Since the interface engineering contributed also to improving stability of PSCs, more studies are required for interface engineering. In PSCs, regardless of n-i-p and p-i-n type, three important interfaces, perovskite/ETL, perovskite/HTL and grain boundary, should be well passivated. Both organic and inorganic materials can be candidates for interface passivation, where selection rule for choosing the materials is required to be developed to reduce trial and error. From the industrial point of view, precursor materials seem to be issued in case of mass production of PSCs. Thus, economic ways to produce high quality precursor materials for PSCs are needed to be developed. For instance, aqueous synthesis of highly pure perovskite precursors is a good example [43].

Data availability No datasets were generated or analyzed during the current study.

Declarations

Conflict of Interest There is no conflict of interest.

References

1. H.-S. Kim, C.-R. Lee, J.-H. Im, K.-B. Lee, T. Moehl, A. Marchioro, S.-J. Moon, R. Humphry-Baker, J.-H. Yum, J.E. Moser, M. Grätzel, N.-G. Park, Sci. Rep. **2**, 591 (2012)
2. NREL best research-cell efficiency chart. https://www.nrel.gov/pv/cell-efficiency.html. Accessed 6 June 2024
3. N.-G. Park, Mater. Today **18**, 65 (2015)
4. N.-G. Park, J. Phys. Chem. Lett. **4**, 2423 (2013)
5. H.S. Jung, N.-G. Park, Small **11**, 10 (2015)
6. D. Weber, Z. Naturforsch. **33b**, 1443 (1978)
7. J.M. Kadro, K. Nonomura, D. Gachet, M. Grätzel, A. Hagfeldt, Sci. Rep. **5**, 11654 (2015)
8. M.I. Saidaminov, A.L. Abdelhady, B. Murali, E. Alarousu, V.M. Burlakov, W. Peng, I. Dursun, L. Wang, Y. He, G. Maculan, A. Goriely, T. Wu, O.F. Mohammed, O.M. Bakr, Nat. Commun. **6**, 7586 (2015)
9. V.M. Goldschmidt, Naturwissenschaften **14**, 477 (1926)
10. A. Leguy, J. Frost, A. McMahon et al., Nat. Commun. **6**, 7124 (2015)
11. A. Poglitsch, D. Weber, J. Chem. Phys. **87**, 6373–6378 (1987)
12. N. Onoda-Yamamuro, T. Matsuo, H. Suga, J. Phys. Chem. Solids **51**, 1383–1395 (1990)
13. A. Kojima, K. Teshima, Y. Shirai, T. Miyasaka, J. Am. Chem. Soc. **131**, 6050–6051 (2009)
14. J.-H. Im, C.-R. Lee, J.-W. Lee, S.-W. Park, N.-G. Park, Nanoscale **3**, 4088 (2011)
15. M.M. Lee, J. Teuscher, T. Miyasaka, T.N. Murakami, H.J. Snaith, Science **338**, 643 (2012)
16. M.A. Green, E.D. Dunlop, M. Yoshita, N. Kopidakis, K. Bothe, G. Siefer, X. Hao, Prog. Photovolt. Res. Appl. **32**, 3 (2024)
17. C. Zhang, K. Wei, J. Hu, X. Cai, G. Du, J. Deng, Z. Luo, X. Zhang, Y. Wang, L. Yang, J. Zhang, A review on organic materials for HTL. Mater. Today **67**, 518 (2023)
18. L. Zang, C. Zhao, X. Hu, J. Tao, S. Chen, J. Chu, A review on inorganic and organic materials for ETL. Small **20**, 2400807 (2024)
19. X. Jing, Z. Zhang, T. Chen, J. Luo, A review on inorganic materials for HTL. Energy Technol. **11**, 2201005 (2023)
20. Y. Yao, C. Cheng, C. Zhang, H. Hu, K. Wang, S. De Wolf, A review on organic HTLs for inverted (p-i-n) PSCs. Adv. Mater. **34**, 2203794 (2022)
21. M. Katayama, M. Shinoda, K. Ozutsumi, S. Funahashi, Y. Inada, Anal. Sci. **28**, 103 (2012)
22. N. Ahn, D.-Y. Son, I.-H. Jang, S.M. Kang, M. Choi, N.-G. Park, J. Am. Chem. Soc. **137**, 8696 (2015)
23. Q. Han, S.-H. Bae, P. Sun, Y.-T. Hsieh, Y.M. Yang, Y.S. Rim, H. Zhao, Q. Chen, W. Shi, G. Li, Y. Yang, Adv. Mater. **28**, 2253 (2016)
24. J.-W. Lee, D.-H. Kim, H.-S. Kim, S.-W. Seo, S.M. Cho, N.-G. Park, Adv. Energy Mater. **15**, 1501310 (2015)
25. M. Saliba, T. Matsui, J.-Y. Seo, K. Domanski, J.-P. Correa-Baena, M.K. Nazeeruddin, S.M. Zakeeruddin, W.R. Tress, A. Abate, A. Hagfeldt, M. Grätzel, Energy Environ. Sci. **9**, 1989 (2016)
26. M. Saliba, T. Matsui, K. Domanski, J.-Y. Seo, A. Ummadisingu, S.M. Zakeeruddin, J.-P. Correa-Baena, W.R. Tress, A. Abate, A. Hagfeldt, M. Grätzel, Science **354**, 206 (2016)
27. M. Stolterfoht, C.M. Wolff, Y. Amir, A. Paulke, L. Perdigón-Toro, P. Caprioglio, D. Neher, Energy Environ. Sci. **10**, 1530 (2017)
28. M.A. Mahmud, N.K. Elumalai, M.B. Upama, D. Wang, A.M. Soufiani, M. Wright, C. Xu, F. Haque, A. Uddin, A.C.S. Appl, Mater. Interfaces **9**, 33841 (2017)
29. H.X. Dang, K. Wang, M. Ghasemi, M.-C. Tang, M. De Bastiani, E. Aydin, E. Dauzon, D. Barrit, J. Peng, D.-M. Smilgies, S. De Wolf, A. Amassian, Joule **3**, 1746 (2019)

30. W. Chen, Y. Zhou, L. Wang, Y. Wu, B. Tu, B. Yu, F. Liu, H.-W. Tam, G. Wang, A.B. Djurišić, L. Huang, Z. He, Adv. Mater. **30**, 1800515 (2018)
31. H.-S. Kim, N.-G. Park, Adv. Mater. **35**, 2204807 (2023)
32. S.Y. Leblebici, L. Leppert, Y. Li, S.E. Reyes-Lillo, S. Wickenburg, E. Wong, J. Lee, M. Melli, D. Ziegler, D.K. Angell, D.F. Ogletree, P.D. Ashby, F.M. Toma, J.B. Neaton, I.D. Sharp, A. Weber-Bargioni, Nat. Energy **1**, 16093 (2016)
33. C. Ma, M.-C. Kang, S.-H. Lee, S.J. Kwon, H.-W. Cha, C.-W. Yang, N.-G. Park, Joule **6**, 2626 (2022)
34. Z. Liang, Y. Zhang, H. Xu, W. Chen, B. Liu, J. Zhang, H. Zhang, Z. Wang, D.-H. Kang, J. Zeng, X. Gao, Q. Wang, H. Hu, H. Zhou, X. Cai, X. Tian, P. Reiss, B. Xu, T. Kirchartz, Z. Xiao, S. Dai, N.-G. Park, J. Ye, X. Pan, Nature **624**, 557 (2023)
35. C. Ma, F.T. Eickemeyer, S.-H. Lee, D.-H. Kang, S.J. Kwon, M. Grätzel, N.-G. Park, Science **379**, 173 (2023)
36. S. Shin, S. Seo, S. Jeong, A.S. Sharbirin, J. Kim, H. Ahn, N.-G. Park, H. Shin, Adv. Sci. **10**, 2300798 (2023)
37. Y. Zhang, T. Yang, S.-U. Lee, S. Liu, K. Zhao, N.-G. Park, ACS Energy Lett. **9**, 159 (2023)
38. N. Rolston, A.D. Printz, J.M. Tracy, H.C. Weerasinghe, D. Vak, L.J. Haur, A. Priyadarshi, N. Mathews, D.J. Slotcavage, M.D. McGehee, R.E. Kalan, K. Zielinski, R.L. Grimm, H. Tsai, W. Nie, A.D. Mohite, S. Gholipour, M. Saliba, M. Grätzel, R.H. Dauskardt, Adv. Energy Mater. **8**, 1702116 (2018)
39. C. Zhu, X. Niu, Y. Fu, N. Li, C. Hu, Y. Chen, X. He, G. Na, P. Liu, H. Zai, Y. Ge, Y. Lu, X. Ke, Y. Bai, S. Yang, P. Chen, Y. Li, M. Sui, L. Zhang, H. Zhou, Q. Chen, Nat. Commun. **10**, 815 (2019)
40. W. Meng, K. Zhang, A. Osvet, J. Zhang, W. Gruber, K. Forberich, B. Meyer, W. Heiss, T. Unruh, N. Li, C.J. Brabec, Joule **6**, 458 (2022)
41. S. Tan, T. Huang, I. Yavuz, R. Wang, T.W. Yoon, M. Xu, Q. Xing, K. Park, D.-K. Lee, C.H. Chen, R. Zheng, T. Yoon, Y. Zhao, H.-C. Wang, D. Meng, J. Xue, Y.J. Song, X. Pan, N.-G. Park, J.-W. Lee, Y. Yang, Nature **605**, 268 (2022)
42. C. Zhang, Y. Son, H. Kim, S.-H. Lee, X. Liang, G. Fu, S.-U. Lee, D.-A. Park, Q. Jiang, K. Zhu, N.-G. Park, Joule **8**, 1 (2024)
43. P. Zhu, D. Wang, Y. Zhang, Z. Liang, J. Li, J. Zeng, J. Zhang, Y. Xu, S. Wu, Z. Liu, X. Zhou, B. Hu, F. He, L. Zhang, X. Pan, X. Wang, N.-G. Park, B. Xu, Science **383**, 524 (2024)